



# Butyl rubber-based interpenetrating polymer networks with side chain crystallinity: Self-healing and shape-memory polymers with tunable thermal and mechanical properties

Esra Su<sup>a</sup>, Gozde Bayazit<sup>b</sup>, Semra Ide<sup>b</sup>, Oguz Okay<sup>a,\*</sup>

<sup>a</sup> Department of Chemistry, Istanbul Technical University, 34469 Maslak, Istanbul, Turkey

<sup>b</sup> Department of Physics Engineering and Department of Nanotechnology and Nanomedicine, Hacettepe University, 06800 Beytepe, Ankara, Turkey

## ARTICLE INFO

### Keywords:

IPNs  
Butyl rubber  
Semicrystalline polymer  
Energy dissipation  
Self-healing  
Shape-memory

## ABSTRACT

A self-healing and shape-memory interpenetrating polymer network (IPN) is produced by UV polymerization of n-octadecyl acrylate (C18A) monomer in a toluene solution of butyl rubber (isobutylene-isoprene rubber, IIR) using Irgacure 2959 photoinitiator at ambient temperature. IPNs containing 20–80 wt% IIR have crystalline domains formed by side-by-side packed octadecyl side chains aligned perpendicular to the poly(C18A) (PC18A) backbone. TEM images reveal that the morphology of IPNs consists of crystalline domains dispersed in a continuous amorphous matrix where the size of the dispersed phase could be adjusted between  $\mu\text{m}$  and  $\text{nm}$  level by changing the amount of IIR. Calculations indicate that the effective cross-link density of IPNs is mainly determined by their crystalline domains followed by hydrophobic associations while the chemical cross-links between IIR and PC18A components are negligible. We also show that the crystalline domains acting as sacrificial bonds dissipate energy under strain leading to a significant toughness improvement. IPNs exhibit tunable melting temperature (46–50 °C), crystallinity (1.5–25%), Young's modulus (0.6–35 MPa), toughness (1.3–12 MPa), and a stretchability of up to 1200% by varying the amount of IIR component. What is more, they also exhibit temperature induced healing behavior with 59–77% efficiency, and an effective shape-memory function. The strategy presented here is applicable for the preparation of IPNs based on various rubbers and poly(n-alkyl (meth)acrylates) with long alkyl side chains.

## 1. Introduction

Elastomers or rubbers are soft polymer networks characterized by their very high stretchability and complete recoverability. These characteristics originate from their flexible and long polymer chains with entropic elasticity, that are joined together into a 3D network structure, usually via covalent sulfur cross-links [1]. One would expect that the replacement of the permanent sulfur cross-links with non-covalent ones that can break and reform reversibly would result in a dynamic elastomeric network with smart functions such as the self-healing ability. In recent years, preparation of physically cross-linked self-healable commercial rubbers with good mechanical properties attracts significant interest to prolong their lifetimes and to reduce waste generation and disposal costs [2]. Moreover, shape-memory is another smart function of elastomers for their various biomedical applications including sensors, flexible electronics, implants, actuators, and smart medical devices [3].

To create self-healing in commercial rubbers, sulfur vulcanization was carried out by adding copper catalysts to trigger disulfide metathesis reaction in vulcanized rubber and hence, to create reversible cross-links [4,5]. By manipulating vulcanization conditions, Hernandez et al. increased the fraction of dynamic disulfide bonds in rubber without modifying the commercial rubber formulation [6,7]. Alternatively, dynamic covalent bonds, hydrogen bonding and ionic interactions were utilized instead of sulfur vulcanization to create reversible cross-links in commercial rubbers [2,8–23]. For instance, functionalization of bromobutyl rubber (BIIR) with butylimidazole creates pendant imidazolium bromide groups on BIIR that are able to form ionic associations serving as reversible cross-links, and providing formation of rubbers with 1000% stretchability and around 9 MPa tensile strength [18]. It was shown that the tensile strength of the ionically cross-linked rubbers decreases while their self-healing efficiency increases as the alkyl chain length of alkyl imidazoles increases [19]. Alternatively, rubber-based

\* Corresponding author.

E-mail address: [okayo@itu.edu.tr](mailto:okayo@itu.edu.tr) (O. Okay).

<https://doi.org/10.1016/j.eurpolymj.2022.111098>

Received 21 October 2021; Received in revised form 7 January 2022; Accepted 26 February 2022

Available online 2 March 2022

0014-3057/© 2022 Elsevier Ltd. All rights reserved.

blends were prepared to create shape-memory and self-healing behavior [24–32]. A shape-memory polymer composite was also designed by swelling vulcanized natural rubber in stearic acid to produce crystalline regions acting as the switching phase of the composite [33].

We recently described a facile and versatile approach for fabrication of butyl rubber-based interconnected interpenetrating polymer networks (IPNs) with shape-memory and temperature-induced healing behavior [34]. They were prepared by dissolving butyl rubber (isobutylene-isoprene rubber, IIR) in the melt of n-octadecyl acrylate (C18A) monomer and Irgacure 2959 initiator followed by UV polymerization at ambient temperature for 1 h. IIR component of the IPN is a biocompatible amorphous ductile polymer consisting of isobutylene and isoprene (1.7 mol%) units while octadecyl side chains of poly(C18A) (PC18A) component form lamellar crystals and provide a convenient way for tuning the mechanical properties. However, the IIR content of IPNs could not be increased above 40 wt% due to the high viscosity of IIR/C18A mixture preventing a complete mixing [34]. As a consequence, thermal and mechanical properties of IPNs cannot be varied over a wide range, and they exhibited a relatively low extensibility (<740%).

Our aim in this work was to fabricate semicrystalline IPNs of IIR and PC18A over a wide range of IIR content. To achieve this aim, toluene was included into the reaction mixture which is a good solvent for both IIR and C18A. IPNs were prepared by dissolving IIR and C18A at various compositions in toluene containing Irgacure 2959 initiator followed by UV polymerization at  $30 \pm 2$  °C for 1 h. As will be seen below, the incorporation of toluene into the reaction system increases the IIR content of IPNs up to 80 wt% leading to a significant decrease in the size of crystalline domains, a much higher stretchability (up to 1200%), and tunable melting temperature (46–50 °C), crystallinity (1.5–25%), Young's modulus (0.6–35 MPa), and toughness (1.3–12 MPa), as compared to IPNs reported in our previous work [34]. What is more, they all exhibit temperature induced healing behavior with 59–77% efficiency, and an effective shape-memory function. The morphology of IPNs is composed of crystalline domains dispersed in a continuous amorphous matrix where the size of the dispersed phase could be adjusted by the amount of IIR. Calculations indicate that the effective

cross-link density of IPNs is mainly determined by their crystalline domains followed by hydrophobic associations while the chemical cross-links between IIR and PC18A components are negligible. We also show that the crystalline domains acting as sacrificial bonds dissipate energy under strain leading to a significant toughness improvement.

## 2. Results and discussion

### 2.1. Formation of IPNs

Semicrystalline IPNs of IIR and PC18A were synthesized by polymerizing C18A monomer in a toluene solution of IIR at  $30 \pm 2$  °C in the presence of Irgacure 2959 initiator under UV light at 360 nm. The IIR content in the IIR + C18A mixture was varied between 20 and 80 wt% while their total concentration was fixed at 74.25 wt% with the rest being the diluent toluene.

We first monitored UV polymerization of C18A in a toluene solution of IIR by rheometry using oscillatory deformation tests. Fig. 1a shows the reaction time dependences of the storage  $G'$  and loss moduli  $G''$ , and the loss factor  $\tan \delta$  ( $=G''/G'$ ) of IIR/PC18A mixture at 30 °C with various IIR contents as indicated. Before switch-on the UV light, i.e., at times less than 2 min, the higher the IIR content in the solution, the higher the  $G'$ , as indicated by an arrow in the figure, due to the increasing viscosity of the reaction system. With the onset of UV polymerization,  $G'$  rapidly increases and approaches to a limiting value within 10 min. DSC measurements revealed that the melting peak of C18A monomer at 30 °C disappeared after a reaction time of 1 h indicating complete conversion of the monomer to PC18A polymer (Fig. S1). Increasing IIR content also increases the modulus  $G'$  from  $10^0$  to  $10^1$  kPa while the loss factor  $\tan \delta$  remains constant at around 0.5. Thus, mechanically weak materials with a modulus of kPa level could be obtained after the in situ polymerization of C18A in IIR solution. However, removing the diluent toluene from as-prepared IPNs followed by cooling to room temperature resulted in a significant increase in the modulus  $G'$  from kPa to MPa level (Table S1). For instance,  $G'$  of the IPN with 20 wt% IIR becomes 13 MPa at a frequency  $\omega$  of  $6.28 \text{ rad}\cdot\text{s}^{-1}$ , as compared to 3.7 kPa measured at its as-prepared state, revealing a 3500x fold increase

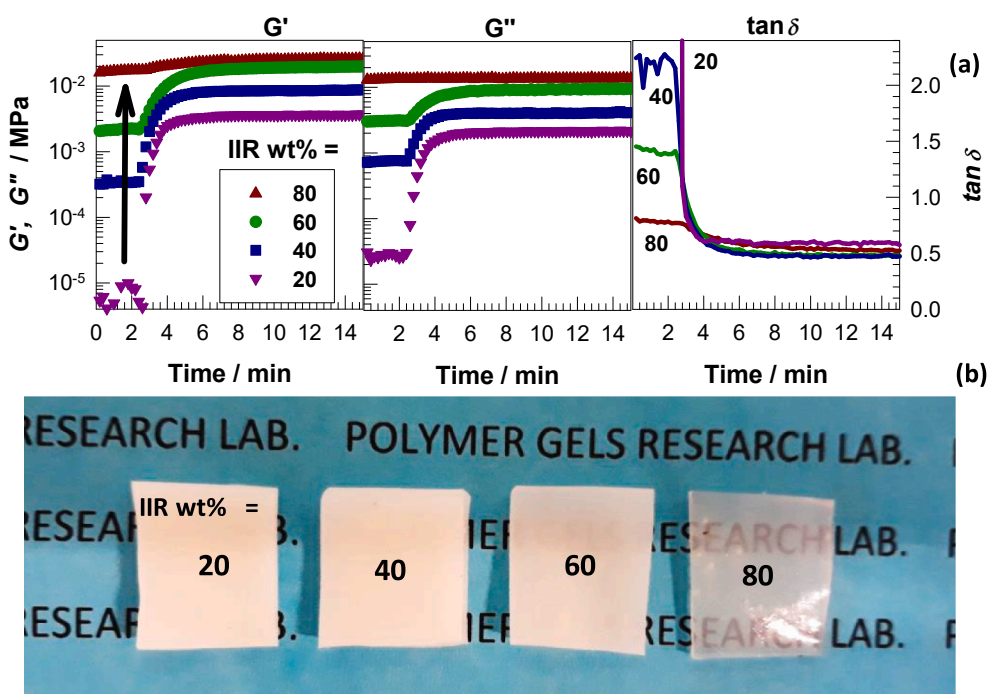


Fig. 1. (a) The reaction time dependences of the storage  $G'$  and loss moduli  $G''$ , and loss factor  $\tan \delta$  during the UV polymerization of C18A in a toluene solution of IIR. IIR contents are indicated. Temperature = 30 °C.  $\gamma_0 = 0.1\%$ .  $\omega = 6.28 \text{ rad}\cdot\text{s}^{-1}$ . (b) Optical images of IPNs with various IIR contents indicated.

in its stiffness. In the following, we discuss the properties of toluene-free IPNs after a reaction time of 1 h.

## 2.2. Microstructure of IPNs

Fig. 1b shows the optical images of IPNs with various IIR contents. The IPN with 20 wt% IIR is opaque while the opacity decreases with increasing IIR content and at 80 wt% IIR, it becomes almost transparent. This indicates occurrence of a phase separation during the polymerization of C18A the extent of which decreases with increasing amount of the rubber IIR. DSC scans of IPNs exhibited melting and crystallization peaks revealing formation of alkyl crystals over the whole range of IIR content. (Fig. 2a, Table S2). The melting temperature  $T_m$  and the degree of crystallinity  $f_{cry}$ , that is, the fraction of C18A units forming lamellar crystals are shown in Fig. 2b as a function of IIR wt% of IPNs. The general trend is that they both decrease from 50 to 46 °C, and from 25 to 1.5 %, respectively, as the IIR amount is increased indicating formation of lesser amount and weaker crystals. The increase in  $T_m$  with increasing IIR content from 20 to 40 wt% can be attributed to the significant decrease in the size of crystalline domains from  $\mu\text{m}$  to nm level increasing thermal stability of alkyl crystals (Fig. 4e). The open symbols in the Fig. 2b represent the data of IPNs prepared by bulk polymerization of C18A [34]. It is seen that the incorporation of toluene in the reaction mixture does not affect much the thermal properties of IPNs in their dried states, but provides tunability of  $T_m$  and  $f_{cry}$  over a wide range. Fig. 3a and Fig. 3b show wide-angle (WAXS) and small-angle X-ray scattering (SAXS) patterns of IPNs, respectively, at various IIR contents between 20 and 80 wt%. WAXS curves reveal a common peak at 21.2° (0.42 nm  $d_1$  spacing) which is typical for semicrystalline PC18A and corresponds to the spacing between two octadecyl (C18) side-chains belonging to the same PC18A backbone (Fig. 3c) [35–38]. SAXS patterns show a broad peak at  $0.08 \text{ \AA}^{-1}$  corresponding to a long-range order with a  $d_2$  spacing of 7.9 nm. As reported by Osada for semicrystalline hydrogels, this spacing is typical for the tail-to-tail arrangement of C18 side chains, i.e., it corresponds to the backbone-to-backbone distance of PC18A chains in the lamellar crystals (Fig. 3c) [38–40]. We should note that the  $d_2$  spacing determined as 7.9 nm is longer than the value of 5–5.45 nm reported by Osada [39]. This is attributed to the steric effect of IIR restricting the alignment of C18 side chains. These characteristic peaks in WAXS and SAXS patterns become weaker and broader with increasing IIR content reflecting decreasing crystallinity and formation of less ordered crystalline domains. A deeper analysis of the SAXS data reveals existence of crystalline nanoaggregations in IPNs increasing in size with increasing IIR content, i.e., their radius of gyration increases from 35 to 42 nm as the content of IIR is increased from 20 to 80 wt%

(Supplementary Text, Fig. S2). Nevertheless, crystal packing and ordered structures are weakening. The crystallinity that deteriorates at large IIR contents and the irregular morphology of nano-formations seem to shrink the micro-sized crystalline domains. This situation may be explained by the interaction between well-ordered nano aggregations which can support large micro-formations at low IIR contents (see below).

Fig. 4(a-d) shows TEM images of IPNs with 20 (a), 40 (b), 60 (c), and 80 wt% IIR (d) at three different magnifications (Scale bars: 5  $\mu\text{m}$  to 0.5  $\mu\text{m}$  from left to right). The images were acquired in bright field (BF, the first two columns), and dark-field modes (DF, last column). In the BF mode, the crystalline domains constituting the dispersed phase appear dark while the amorphous matrix seems bright, and vice versa for the DF mode [34]. The morphology of IPNs consists of dispersed crystalline particles in a continuous amorphous matrix. As the amount of IIR is increased, the dispersed phase morphology changes from more or less spherical large domains into fish-shaped ones of much smaller dimensions, and finally nanosized spheres.

Moreover, the size of the particles strongly depends on the IIR content, as seen in Fig. 4e showing the distribution of the sphere-equivalent diameters  $D$  of the particles. The number-average particle diameters are  $2.3 \pm 0.2 \mu\text{m}$ ,  $580 \pm 26 \text{ nm}$ ,  $147 \pm 13 \text{ nm}$ , and  $75 \pm 20 \text{ nm}$  for IPNs with 20, 40, 60, and 80 wt% IIR, respectively. We should note that the images of IPNs with 80 wt% IIR were blurry with low resolution so that the actual average diameter maybe smaller than the reported one. Thus, the size of the dispersed crystalline domains can be adjusted between  $\mu\text{m}$  and nm level by changing the IIR content of IPNs. The decrease of the particle diameter with increasing IIR content is attributed to the simultaneous increase of the viscosity of IIR solution in toluene (Fig. 1a). During the photopolymerization of C18A in this solution, the translational diffusion of the growing PC18A radical chains as well as the agglomeration of phase separated crystalline domains are increasingly hindered as the IIR content is increased leading to the formation smaller particles in IPNs.

Fig. 5(a-c) shows scanning TEM (STEM) images of IPN specimens with 20, 40, and 60 wt% IIR, respectively, in DF mode, and the corresponding energy-dispersive X-ray spectroscopy (EDX) elemental maps of carbon (C, red), oxygen (O, blue), and their overlapping areas (purple). Because oxygen atoms only exist in PC18A component, its spatial distribution can be visualized by oxygen mapping. The localization of C and O atoms is seen in the dispersed crystalline phase although they both distribute over the whole investigated area. This finding reveals that the continuous phase is composed of an amorphous interpenetrated network of PC18A and IIR, in which the crystalline domains are distributed. In accord with the TEM images, the size of these domains decreases with

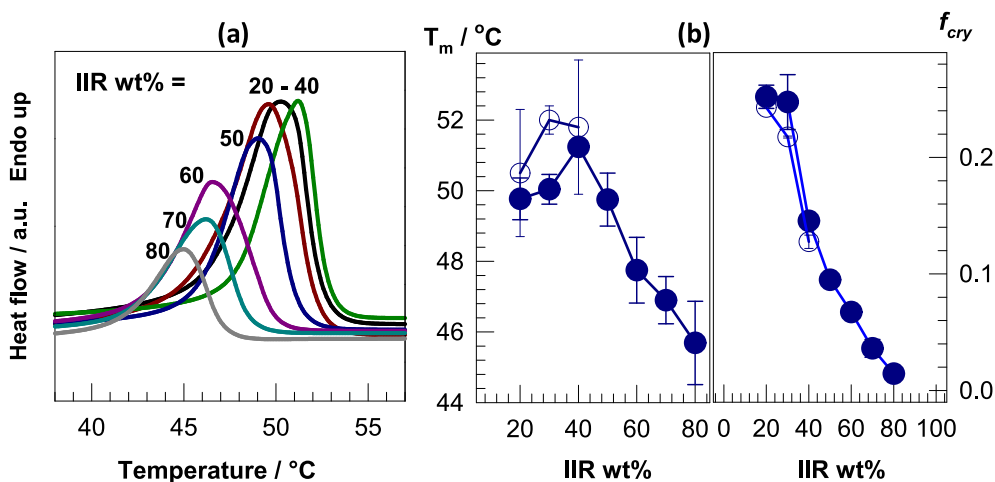
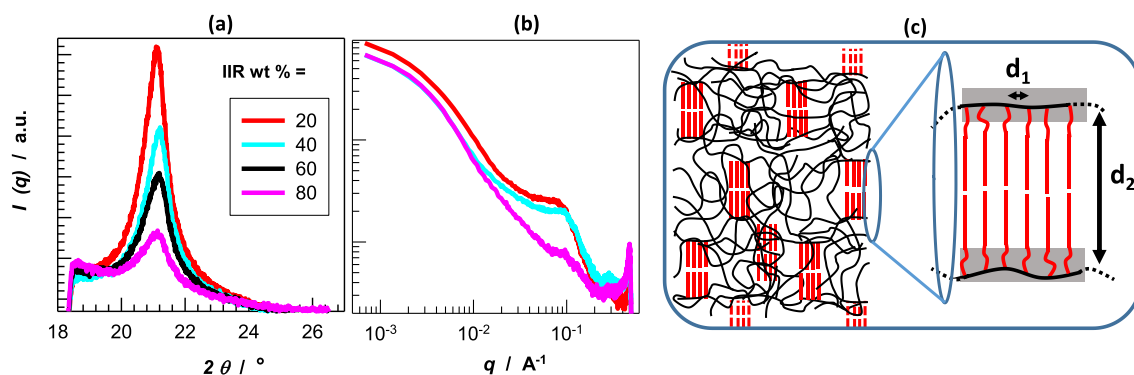
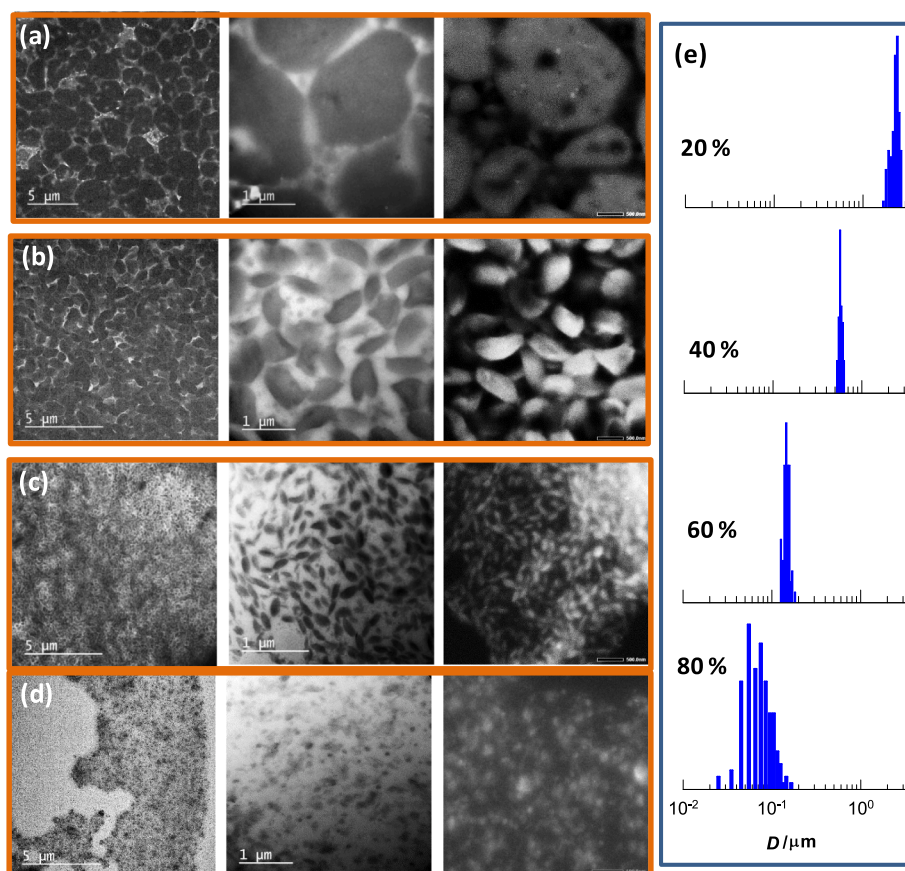


Fig. 2. DSC scans (a), melting temperature  $T_m$  and the degree of crystallinity  $f_{cry}$  (b) of IPNs at various IIR wt%. The open symbols in (b) represent the data for the IPNs prepared without toluene.



**Fig. 3.** WAXS (a) and SAXS patterns (b) of IPNs at various IIR contents, and a scheme showing the microstructure of crystalline domains in IPNs (c). Red vertical lines in (c) represent crystallized side C18 chains while the gray area indicate PC18A backbone and non-crystalline part of the side chains. The spacings  $d_1$  and  $d_2$  are indicated. (For interpretation of the references to colour in this figure legend, the reader is referred to the web version of this article.)



**Fig. 4.** (a-d) TEM images of IPNs with 20 (a), 40 (b), 60 (c), and 80 wt% IIR (d) at three different magnifications. The images were acquired in bright field (BF, the first two columns), and dark-field modes (last column). Scale bars are 5, 1, and 0.5  $\mu\text{m}$  from left to right. (e) The distribution of sphere-equivalent diameters  $D$  of the particles in IPNs with various IIR contents as indicated.

increasing amount of IIR until they become invisible to EDX at 80 wt% IIR (Fig. S3). This change in morphology is also reflected in the optical images of IPNs, showing decreasing opacity with increasing IIR wt% until becoming almost transparent at 80 wt% (Fig. 1b).

The existence of lamellar crystals was also verified by monitoring the modulus  $G'$  of IPNs during a cooling-heating cycle within the rheometer. Fig. 6a shows  $G'$  of IPNs with 20–80 wt% IIR during a thermal cycle between below and above  $T_m$  or  $T_{cry}$ , which consists of 5 steps: (i) isothermal at 65  $^{\circ}\text{C}$  ( $T > T_m$ ) for 10 min, (ii) cooling from 65 to 25  $^{\circ}\text{C}$  ( $T < T_m$ ) at a rate of 2 K/min, (iii) another isothermal at 25  $^{\circ}\text{C}$  for 10 min, (iv) reheating to 65  $^{\circ}\text{C}$  at the same rate, and (v) final isothermal at 65  $^{\circ}\text{C}$ .

The temperature profile of the thermal cycle between 65 and 25  $^{\circ}\text{C}$  is also shown in the figure by the red curve. IPNs undergo up to three-orders of magnitude change in  $G'$  during the thermal cycle, and this change occurs totally reversible. A similar reversible change during the thermal cycle was also observed in the loss modulus  $G''$  (Fig. S4). The transition temperatures during the cooling-heating cycle correspond to the  $T_m$  and  $T_{cry}$  temperatures of IPNs (Fig. S5). The extent of the modulus variation between below and above  $T_m$  or  $T_{cry}$  increases as the IIR content is decreased, similar to the increase of the crystallinity degree (Fig. 2b). Such a drastic and reversible change in the modulus depending on the temperature is known to be important in various applications

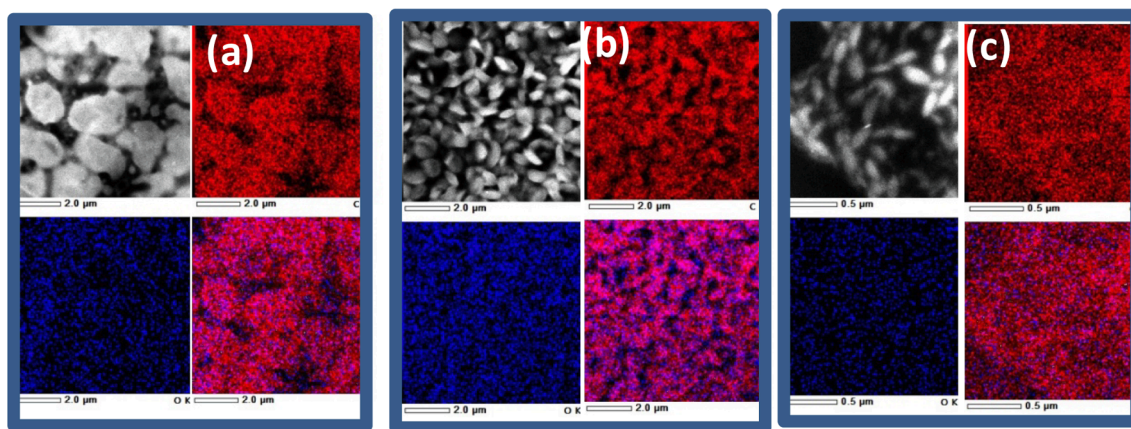


Fig. 5. STEM images and EDX maps of IPNs with 20 (a), 40 (b), and 60 wt% IIR (c). Scale bars: 2  $\mu\text{m}$  (a, b), and 0.5  $\mu\text{m}$  (c).

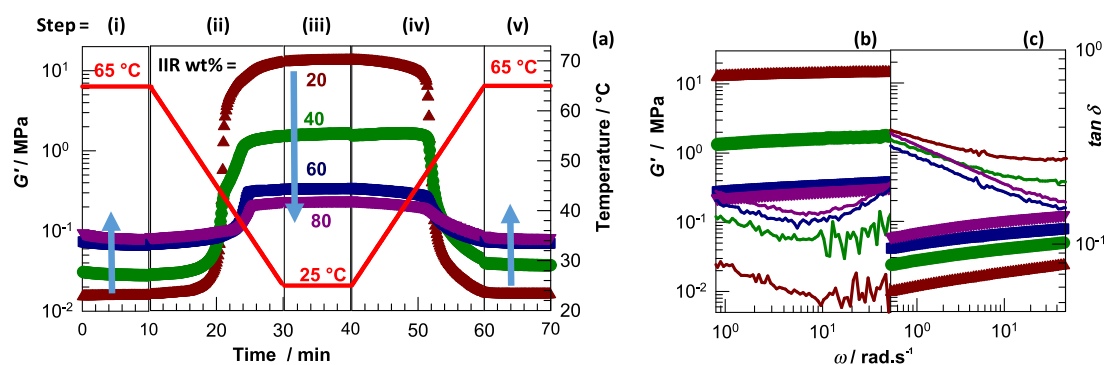


Fig. 6. (a)  $G'$  of IPNs during a cooling-heating cycle between 65 and 25  $^{\circ}\text{C}$ . The temperature profile of the thermal cycle is shown by the curve. Arrows indicate increasing IIR content. Rubber contents are indicated.  $\omega = 6.28 \text{ rad}\cdot\text{s}^{-1}$ ,  $\gamma_0 = 0.1\%$ . (b, c) Frequency dependence of  $G'$  (symbols) and  $\tan \delta$  (curves) of IPNs at 25 (b) and 65  $^{\circ}\text{C}$  (c). IIR = 20 (dark red), 40 (dark green), 60 (dark blue), and 80 wt% (purple).  $\gamma_0 = 0.1\%$ . (For interpretation of the references to colour in this figure legend, the reader is referred to the web version of this article.)

such as 3D/4D printing, electrospinning, and shape-memory. Moreover, IIR content of IPNs affects oppositely on the modulus variation at 65 and 25  $^{\circ}\text{C}$ , as indicated by arrows in Fig. 6a. At 25  $^{\circ}\text{C}$ ,  $G'$  decreases with increasing IIR wt% because of the decreasing degree of crystallinity while it increases at 65  $^{\circ}\text{C}$  due to the increasing viscosity. Fig. 6 (b, c) shows frequency ( $\omega$ ) - dependences of  $G'$  (symbols) and  $\tan \delta$  (curves) of IPNs at 25 (b) and 65  $^{\circ}\text{C}$  (c). At 65  $^{\circ}\text{C}$ ,  $G'$  exhibits a power law increase with  $G' \sim \omega^{0.16 \pm 0.02}$  while those at 25  $^{\circ}\text{C}$  are almost independent on the frequency (exponent =  $0.07 \pm 0.02$ ). Thus, the storage modulus significantly decreases while the viscous character of IPNs increases with rising temperature due to the crystallized octadecyl (C18) side chains that melt and reform during the thermal cycle.

The results thus show the existence of alkyl crystals in IPNs acting as physical cross-links and responsible for their high modulus at 25  $^{\circ}\text{C}$ . Because  $\tan \delta$  remains below unity at above  $T_m$ , other types of cross-links may also exist in IPNs, i.e., those due to the hydrophobic associations between non-crystalline C18A side chains, and chemical links between the isoprene units of IIR and PC18A chains. We should note that, as compared to IPNs prepared by bulk polymerization of C18A [34], present IPNs formed by solution polymerization in toluene exhibit a larger degree of swelling in toluene and a larger amount of soluble species (Table S3, Fig. S6). This reflects a decrease in the number of chemical cross-links formed between the unsaturated groups of IIR chains and the growing PC18A radicals during polymerization. As detailed in the supporting information section, the contribution of these three types cross-links to the effective cross-link density of IPNs was estimated from their modulus  $G'$  measured at 25 and 65  $^{\circ}\text{C}$ , equilibrium swelling ratios, and soluble fractions using the rubber elasticity and equilibrium swelling

theories (Supplementary Text, Fig. S7). It was found that the chemical cross-link density of IPNs is one-order of magnitude smaller than those formed by bulk polymerization of C18A (Fig. S7a). Assuming that each unsaturation of IIR units produces two elastically effective cross-links in IPN, the theoretical chemical cross-link density would be 110–220  $\text{mol}\cdot\text{m}^{-3}$  as compared to 0.4–0.9  $\text{mol}\cdot\text{m}^{-3}$  estimated from their swelling degrees (Supplementary Text). This low chemical cross-linking efficiency can be attributed to the existence of grafted PC18A chains to IIR chains due to the steric effect. The alkyl crystals act as the main cross-linker by forming 68–100% of the total elastically effective cross-links in IPNs. The number of cross-links due to the hydrophobic associations increases with IIR content due to the restriction in the alignment of PC18A chains in the rubber environment (Fig. S7b). From these findings, we can conclude that there are almost no intermolecular chemical cross-links between IIR and PC18A components of the IPNs. Hence, PC18A chains in the IIR matrix form hydrophobic associations and lamellar crystals with each other to generate an IPN structure.

### 2.3. Mechanical properties and smart functions

The mechanical properties of IPNs were measured at  $23 \pm 2$   $^{\circ}\text{C}$  using uniaxial tensile tests at a fixed strain rate of  $5 \text{ min}^{-1}$ . Fig. 7a shows the stress-strain curves in terms of the nominal stress  $\sigma_{nom}$  (force acting per unit area of the undeformed specimen) plotted against the nominal strain  $\epsilon$  (length change of the sample divided by its original length). The IPN containing 20 wt% IIR exhibits a brittle fracture at  $81 \pm 4$  % elongation while all other samples show yielding behavior at around 50% elongation which is accompanied by a strain softening followed by

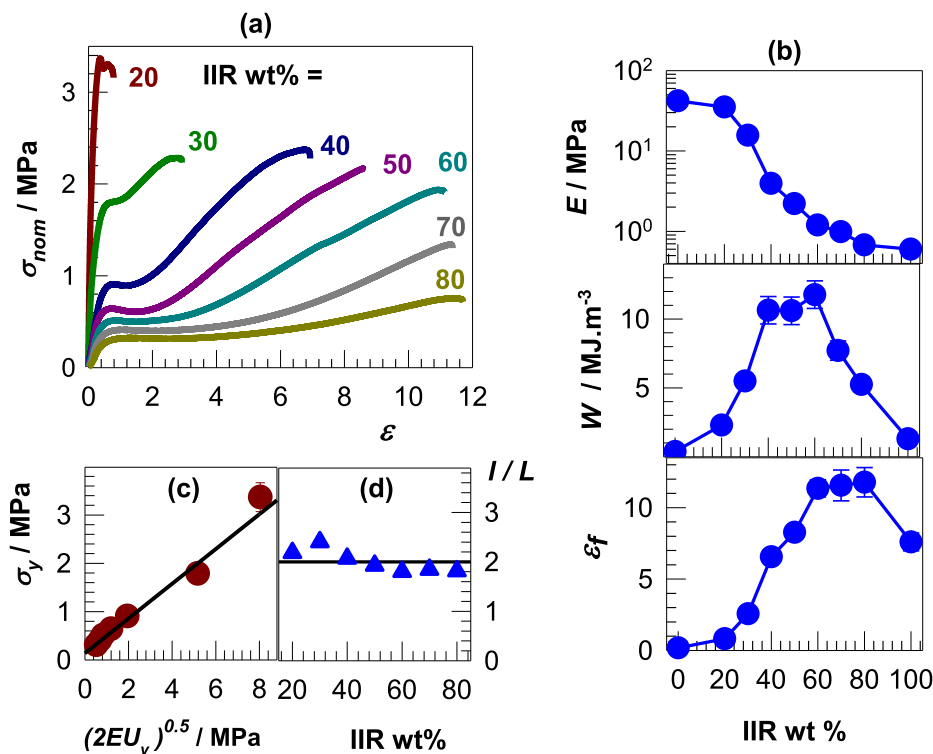


Fig. 7. (a, b) Stress–strain curves (a) and the tensile mechanical parameters (b) of IPNs with various IIR contents. Most of the symbols in (b) are larger than the error bars. (c)  $\sigma_y$  vs  $\sqrt{2EU_y}$  data of IPNs. The solid line is the best fit to Eq. (1). (d) Variation of  $l/L$  ratio with IIR wt%.

strain hardening, leading to a significant stretchability and toughness improvement. We should note that the strain softening regime in the stress–strain curves disappears when the true stress  $\sigma_{true}$  ( $=\lambda \sigma_{nom}$ ) is plotted against the true strain  $\ln \lambda$ , where  $\lambda$  is the elongation ratio (Fig. S8). This reveals that the strain softening is not real, and is an artifact of the nominal strain  $\epsilon$  comparing the sample length with its initial length over the whole range of elongation. In Fig. 7b, Young's modulus  $E$ , toughness  $W$  (area under the stress–strain curve), and elongation at break  $\epsilon_f$  of IPNs are plotted against IIR wt%. The data of IIR and PC18A components alone are also shown in the figures. Increasing IIR content also increases the elongation at break while the modulus  $E$  decreases, which is attributed to the decreasing crystallinity of IPNs. The IPN with 60 wt% IIR exhibits the maximum toughness of  $12 \pm 1$  MJ.m<sup>-3</sup>, together with a high modulus ( $1.2 \pm 0.1$  MPa), and elongation at break ( $1135 \pm 60$  %). Fig. 7b and Table S2 also show that the mechanical parameters of IPNs can be tuned over a wide range by changing the IIR content.

We attribute the toughness improvement in IPNs with increasing IIR wt% to the antagonistic mechanical properties of their components, namely the brittle PC18A component fracturing at a low strain by dissipating energy, and the ductile IIR component gluing the microscopically fractured sample together. Semicrystalline polymers are known to exhibit a morphology composed of stacks of lamellar crystals that are sandwiched between amorphous layers. This morphology leads to the restriction of crystal growth in directions normal to the surface of the amorphous layer, and hence formation of spatially alternating crystal and amorphous layers in polymers [41]. In the present IPN system, stacks of PC18A crystals of around 8 nm in thickness ( $d_2$  spacing) are separated by amorphous regions of higher mobility that are composed of PC18A backbones, non-crystallizable C18A side chains together with IIR chains (Fig. 3c). Under the application of a strain, the relatively mobile chains in the amorphous layer would unfold to form active tie chains interconnecting the lamellar crystal stacks [42–46]. At the yield point, at which IPN loses its stiffness, the stacks of crystals split into pieces with a minimum dimension being equal to that of a single

polymer chain [44–46]. This condition is given by  $l/L = 2$  where  $l$  is the spacing between two successive tie chains bridging the lamellar crystal stacks of thickness  $L$ . According to Nitta and co-workers, the yield stress  $\sigma_y$  of semicrystalline polymers is related to  $l/L$  by [44],

$$\sigma_y = 2\sqrt{2EU_y}(L/l)^2 \quad (1)$$

where  $U_y$  represents the yield energy, i.e., the area below the stress–strain curve up to the yield strength. Fig. 7c presenting  $\sigma_y$  vs  $\sqrt{2EU_y}$  data of IPNs reveals that Eq. (1) provides a good fit to the experimental data. The  $l/L$  ratio was calculated as  $2.0 \pm 0.2$  indicating that stacks of PC18A crystals break down at the yield point into fragments of molecular sizes (Fig. 7d). Thus, the microscopic failure at a low strain (around 50%) produces fragments of PC18A crystals while the amorphous IIR component keeps the IPN sample together leading to a high extensibility and toughness. The mechanism of toughness improvement is thus similar to that of double-network hydrogels composed of brittle and ductile components [47]. Moreover, the strain hardening behavior at high strains is attributed to the alignment of fragmented crystals to the direction of the applied strain producing ordered clusters and hence strengthening IPNs under large strains.

To investigate the extent of energy dissipation under large strains, five successive tensile mechanical cycles up to a maximum strain of 500% were conducted on IPNs at a fixed strain rate of  $5 \text{ min}^{-1}$ . The results are shown in Fig. 8a and Fig. 8b for IPNs with 40 and 80% IIR, respectively, where the solid and dotted curves represent loading and unloading curves. As expected from the occurrence of an internal damage in IPNs at the yield point, the first unloading curve strongly deviates from the loading one with a large hysteresis energy  $U_{hys}$  (the area enveloped by the loading and unloading curves). However, the following cycles are close to reversible, that is each loading or unloading curve of the 2nd to 5th cycle follows the previous one. In accord with this finding, the large residual deformation appearing after the first cycle remains almost unchanged during the following cycles ( $230 \pm 20$  %, and  $150 \pm 20$  % for 40 and 80 wt% IPN, respectively.). Fig. 9a shows  $U_{hys}$ ,

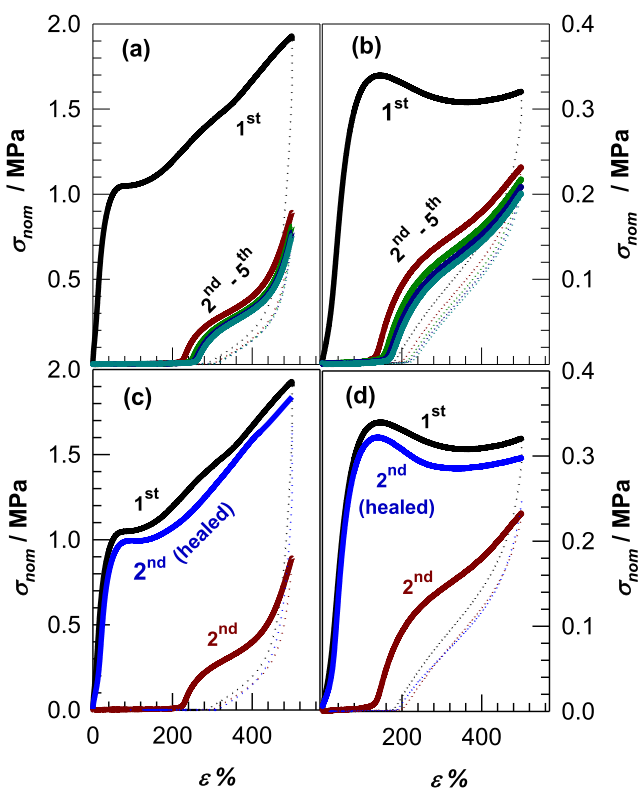


**Fig. 8.** (a, b) Five successive tensile cycles up to a maximum strain  $\varepsilon_{\max}$  of 500% conducted on IPNs with 40 (a) and 80 wt% IIR (b). Strain rate =  $5 \text{ min}^{-1}$ . The solid and dotted curves represent loading and unloading curves. (c, d) Two successive tensile cycles up to  $\varepsilon_{\max} = 500\%$  for IPNs with 40 (c), and 80 wt% IIR (d). The blue curves represent the second loadings after healing of the specimens by the heating-cooling treatment. (For interpretation of the references to colour in this figure legend, the reader is referred to the web version of this article.)

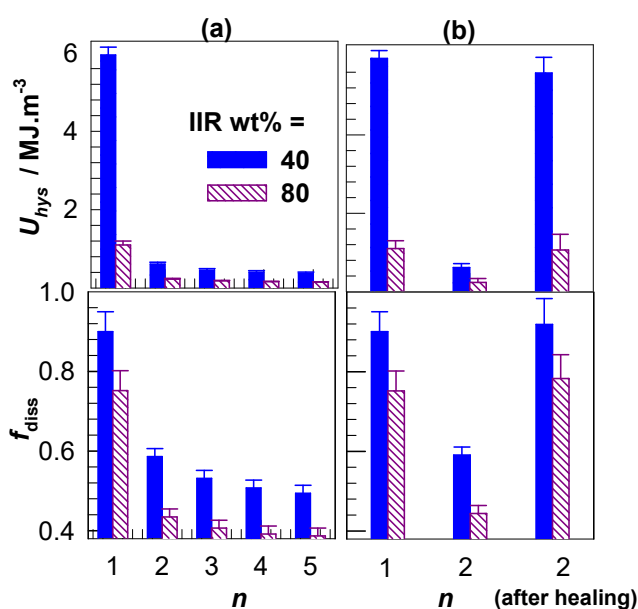


**Fig. 9.** (a) Hysteresis energy  $U_{\text{hys}}$  and the fraction  $f_{\text{diss}}$  of dissipated energy per loading energy plotted against the cycle number  $n$  for IPNs with 40 and 80 wt% IIR. (b)  $U_{\text{hys}}$  and  $f_{\text{diss}}$  values of two successive cycles. The second cycle was conducted before and after healing of the specimens by heating-cooling treatment.

and the fraction  $f_{\text{diss}}$  of dissipated energy per loading energy plotted against the cycle number  $n$  for 40 and 80% IPN samples, respectively. For the sample with 40 wt% IIR,  $U_{\text{hys}}$  in the first cycle is  $5.9 \pm 0.2 \text{ MJ}\cdot\text{m}^{-3}$  while in the following 4 cycles it remains constant at  $0.5 \pm 0.1 \text{ MJ}\cdot\text{m}^{-3}$ . A similar behavior is observable for the sample with 80 wt% IIR ( $1.1 \pm 0.1$  vs  $0.18 \pm 0.03 \text{ MJ}\cdot\text{m}^{-3}$ ).

These findings reveal that the alkyl crystals break down irreversibly during the first loading while the associations between C18A side chains act as reversible cross-links. Breaking and reformation of hydrophobic associations are thus responsible for the reversibility of the 2nd to 5th cycles. According to this scenario, heating the microscopically fractured IPN above  $T_m$  of the alkyl crystals followed by cooling to room temperature will repair the broken crystals and hence recover the original stress-strain curve. To check this point, IPN specimens after the first cycle were first heated at  $65^\circ\text{C}$  for 5 min and then cooled to room temperature before subjecting to the second loading. The blue curves in Fig. 8c and Fig. 8d represent second loading curves of healed IPN samples with 40 and 80 wt% IIR, respectively. It is seen that the second loading after healing closely follows the first one; comparison of  $U_{\text{hys}}$  and  $f_{\text{diss}}$  values also reveal almost complete recovery of the original microstructure (Fig. 9b). The temperature induced recoverability of the microstructure of IPNs indicates that they will have the ability to self-heal after damage.

Macroscopic healing tests indeed demonstrated that all IPNs exhibit recoverability in their microstructure when heated above  $T_m$  of the alkyl crystals. The healing tests were conducted by cutting IPN specimens into two parts and then joining the parts together followed by heating to  $65^\circ\text{C}$  for 24 h and finally cooling to room temperature. The highest healing efficiency was observed for the IPN with 80 wt% IIR; the fracture of this IPN always occurred at any location of the samples. For instance, Fig. 10a shows the images of an IPN specimen with 80 wt% IIR during tensile testing where the dashed red square represents the healed area. The specimen breaks at a location far away from the red area revealing a complete healing of the cut region. Another interesting observation for all IPNs is the appearance of an opacity in the healed area which slowly disappeared with time. The inset to Fig. 10a shows this behavior for an IPN sample with 40 wt% IIR where the healed area at  $65^\circ\text{C}$  becoming opaque after healing are indicated by the dashed red circle. This is attributed to the increased mobility of C18 side chains located at the cut surface at the elevated temperature. The accumulation of the side chains at the damaged area followed by cooling results in the reformation of alkyl crystals bringing the surfaces together and hence initiating the heating induced healing process.

The solid and dashed curves in Fig. 10b present the stress-strain curves of original and healed IPN samples, respectively. The healing was conducted by cut-and-heal treatment at  $65^\circ\text{C}$  for 24 h. In Fig. 10c, the modulus  $E$ , fracture stress  $\sigma_f$ , and elongation at break  $\varepsilon_f$  of original (solid bars) and healed IPNs (dashed bars), and the healing efficiencies (symbols) are plotted against IIR wt%. The reappearance of the yield point after healing and hence, a significant healing is observable indicating reformation of lamellar crystals. The healing efficiencies  $\varepsilon_h$  with respect to  $E$ ,  $\sigma_f$ , and  $\varepsilon_f$  are higher than  $77 \pm 5$ ,  $51 \pm 3$ , and  $59 \pm 2\%$ , respectively. Interestingly, the most efficient healing occurs in the modulus of IPNs revealing recovery of the original microstructure. We may attribute the lower efficiencies in the recovery of the original stress-strain curves to incomplete overlap of the cut surfaces of the damaged specimens.

In addition to the temperature-induced healing, all IPNs exhibited shape-memory effect triggered by temperature. This is due to the existence of C18 crystals acting as the switching segments by locking the temporary shape, and hydrophobic associations as the netpoints determining the permanent shape. We observed a complete recovery of the permanent shape within 20 s by immersing IPN specimens in a temporary shape into water at  $65^\circ\text{C}$  (Fig. 11a). Fig. 11b demonstrates the applications of an IPN specimen as a five-fingered robot hand carrying a

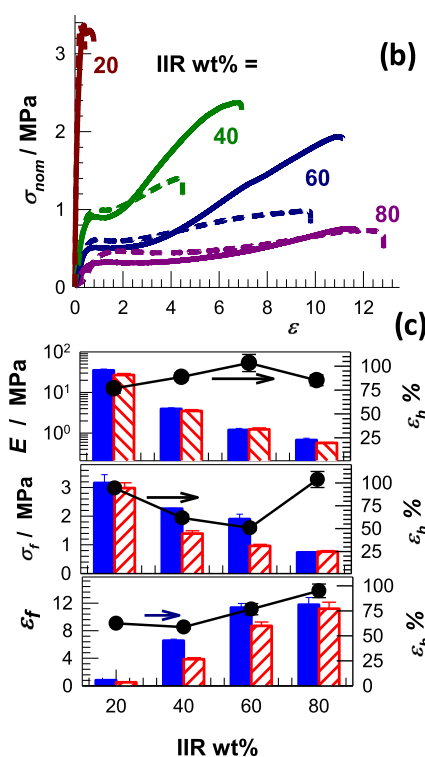
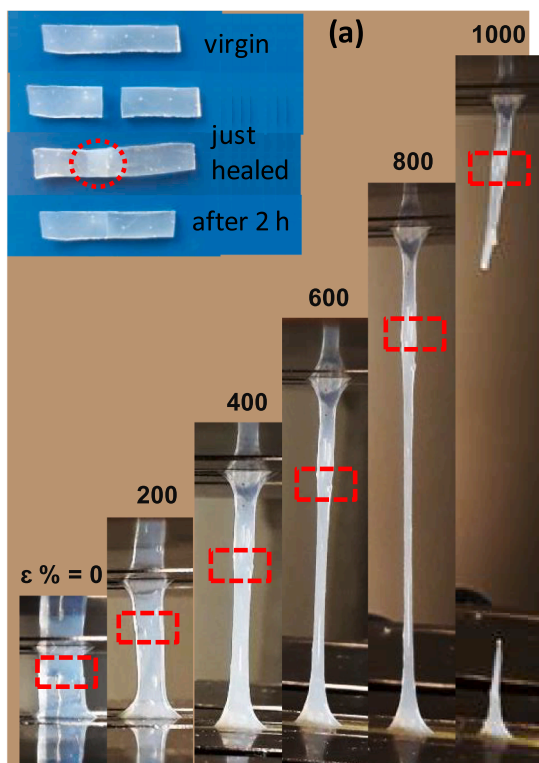


**Fig. 10.** (a) Images of an IPN specimen with 80 wt% IIR during tensile testing. The dashed red square represents the healed area. The specimen breaks at a location far away from the red area revealing a complete healing of the cut region. The inset shows the appearance of opacity in the healed area (dashed red circle) for an IPN sample with 40 wt% IIR. (b)  $\sigma_{nom}$  vs.  $\epsilon$  plots of original and healed samples shown by the solid and dashed curves, respectively. (c)  $E$ ,  $\sigma_f$ , and  $\epsilon_f$  of original (solid bars) and healed IPNs (dashed bars), and their healing efficiencies  $\epsilon_h$  (symbols) plotted against IIR wt%. (For interpretation of the references to colour in this figure legend, the reader is referred to the web version of this article.)

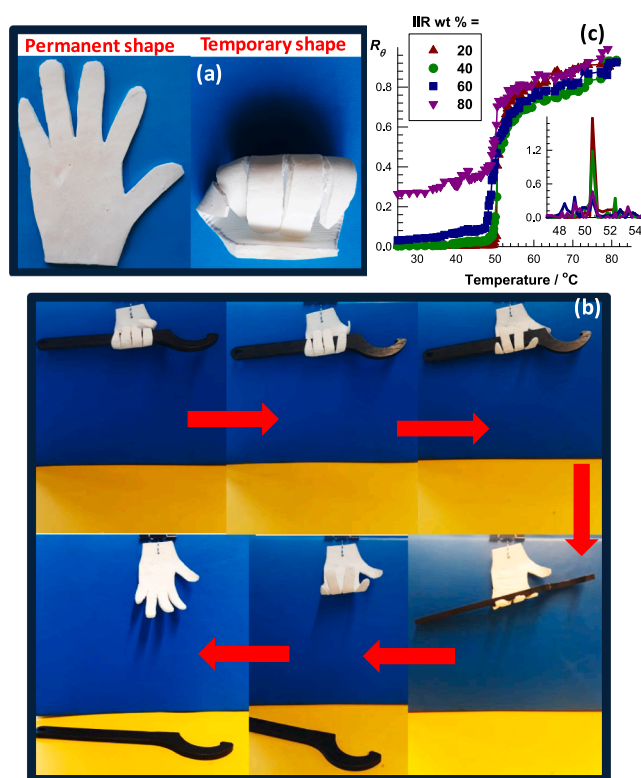


**Fig. 11.** (a) An IPN specimen with 40 wt% IIR in its permanent and temporary shapes. A complete recovery of the permanent shape occurs within 20 s by immersing the sample in the temporary shape into water at 65 °C. (b) An IPN sample with 40 wt% IIR as a five-fingered robot hand carrying a wrench of 156 g in mass, and dropping it to the ground when heated to 65 °C. (c) The shape-recovery ratio  $R\theta$  of IPNs plotted against the temperature. The inset shows the derivative of  $R\theta$  with respect to temperature plotted against the temperature.

wrench of 156 g in mass, and dropping it to the ground when heated to 65 °C (supplementary Movie). The robot hand is in permanent open-hand shape and it is transformed to the temporary closed-hand shape prior to the operation. Fig. 11c shows the shape-recovery ratio  $R\theta$  of IPNs plotted against the temperature. Except for the sample with 80 wt% IIR, all IPNs fix their temporary shapes up to around 48 °C reflecting the effect of the crystallinity degree on the shape-fixity ratio. Thus a  $f_{CRY}$  value of at least 7% suffices to achieve a complete shape-fixity ratio. Moreover, a shape-recovery ratio of above 80% was reached for all IPNs at 50 °C. The inset to Fig. 11c shows the derivative of  $R\theta$  with respect to temperature plotted against the temperature. For all IPNs, the maximum rate of change of  $R\theta$  is reached at 50.6 °C while its magnitude decreases with increasing IIR content, i.e., with decreasing crystallinity.

#### 2.4. Suitability of the term IPN for the present materials

A simple definition of IPN is a system consisting of two cross-linked polymer networks that are physically entangled but not chemically linked [48–50]. Moreover, interconnected IPN (c-IPN) is a specific class of IPN that also includes chemical cross-links between the two network components. Throughout this work, we call the present materials as IPNs, more specifically, non-interconnected interpenetrating IIR and PC18A networks containing phase separated nanocrystalline domains due to the following reasons. As detailed in the previous sections, the polymerization of C18A proceeds in a toluene solution of 20–80 wt% IIR. Thus, the growing PC18A radicals in the presence of IIR chains may attack to the unsaturated isoprene units of IIR chains to form chemical cross-links. However, swelling and gel fraction measurements indicate that the contribution of the chemical cross-links  $v_{e,chem}$  to the total cross-link density  $v_e$  of IPNs is less than 0.1% (Supplementary Text, Figs. S6 and S7). Thus, the cross-link density of IPNs is mainly determined by the physical cross-links due to the crystalline domains and hydrophobic associations. Calculations using the rubber elasticity theory together with the storage moduli of IPNs at below and above  $T_m$  reveal that the contribution of physical cross-links due to the crystalline domains decreases from 99.9 to 68% while that due to the hydrophobic associations

increases from 0.1 to 32% (Fig. S7). Because these effective physical cross-links can only exist between PC18A chains, a physically cross-linked PC18A network forms within a second network of IIR with chain entanglements entrapped in the intercrystalline domains of IPNs.

The degree of crystallinity  $f_{cry}$  of IPNs decreases from 25 to 1.5% as the IIR content is increased from 20 to 80 wt% (Fig. 2b). This means that only 1.5–25 mol% of C18A units are in crystalline domains, with the rest being in the amorphous phase together with the IIR chains. The EDX maps indeed show the distribution of PC18A component over the whole IPN specimens (Fig. 5). All these findings reveal the presence of interpenetrating IIR and PC18A networks forming the continuous phase of IPN containing phase separated nanocrystalline domains. It might be argued that the present materials may also be called amphiphilic polymer conetworks (APCNs) made via the macro-crosslinker approach [51,52]. According to this definition, the present materials should consist of IIR chains with PC18A branches comprising a few C18A repeat units. We determined the number average molecular weight of PC18A formed under the same experimental condition but in the absence of IIR as 90,000 g·mol<sup>-1</sup> with a very broad polydispersity index of 20 [34]. Thus, the relatively long chain length of PC18A component and its existence in both continuous and nanocrystalline domains eliminate this definition.

### 3. Conclusions

Preparation of physically cross-linked self-healable and shape-memory commercial rubbers with good mechanical properties attracts significant interest not only to prolong their lifetimes and to reduce waste generation and disposal costs, but also for their various biomedical applications including sensors, flexible electronics, implants, actuators, and smart medical devices. We recently described a facile and versatile approach for fabrication of IIR-based IPNs with shape-memory and temperature-induced healing behavior. They were prepared by polymerizing C18A in the presence of IIR under UV light at ambient temperature. However, the IIR content of IPNs could not be increased above 40 wt% due to the high viscosity of IIR/C18A mixture preventing a complete mixing. Here, we demonstrate the fabrication of self-healing and shape-memory semicrystalline IPNs of IIR and PC18A over a wide range of IIR content. IPNs were prepared by dissolving IIR and C18A at various compositions in toluene containing Irgacure 2959 initiator followed by UV polymerization at 30 ± 2 °C for 1 h. WAXS and SAXS data show the existence of lamellar crystals in IPNs by the alignment of C18 side chains to form a backbone-to-backbone distance of 7.9 nm. The morphology of IPNs consists of crystalline domains dispersed in a continuous amorphous IPN of PC18A and IIR. As the content of IIR is increased, the dispersed phase morphology changes from more or less spherical large domains into fish-shaped ones of much smaller dimensions, and finally nanosized spheres. The size of the dispersed phase decreases from μm to nm level with increasing amount of IIR due to the increase of viscosity. Calculations indicate that the effective cross-link density of IPNs is mainly determined by their crystalline domains followed by hydrophobic associations while the chemical cross-links between IIR and PC18A components are negligible. We also show that the crystalline domains acting as sacrificial bonds dissipate energy under strain leading to a significant toughness improvement. IPNs exhibit tunable melting temperature (46–50 °C), crystallinity (1.5–25%), Young's modulus (0.6–35 MPa), toughness (1.3–12 MPa), and a stretchability of up to 1200% by varying the amount of IIR component. They also exhibit temperature induced healing behavior with 59–77% efficiency, and an effective shape-memory function. The strategy presented here is applicable for the preparation of IPNs based various rubbers and poly(n-alkyl(meth)acrylates) with long alkyl side chains.

## 4. Experimental section

### 4.1. Materials

One of the main components of IPNs is butyl rubber purchased from Nizhnekamskneftekhim, Russia, which was purified by reprecipitation from toluene solution in methanol followed by drying to constant mass. The unsaturation degree of butyl rubber (IIR) used in this work was 1.7 ± 0.2 mol%, as determined by <sup>1</sup>H NMR [34]. The number-average molecular weight  $\bar{M}_n$  of IIR was determined as 3.2 × 10<sup>5</sup> g·mol<sup>-1</sup> (PDI = 2.1) on a gel permeation chromatograph (Malvern GPC Max, RI detector, mobile phase: THF) using polystyrene standards (PolyCal, Malvern). n-Octadecyl acrylate (C18A) monomer, 2-hydroxy-4'-(2-hydroxyethoxy)-2-methylpropiophenone (Irgacure 2959) photoinitiator were obtained from Sigma-Aldrich (St. Louis, MO) and used as received.

IPNs were prepared by UV polymerization of C18A using Irgacure 2959 photoinitiator at 360 nm in a toluene solution of IIR. The IIR content in the IIR + C18A mixture was varied between 20 and 80 wt% while their total concentration was fixed at 74.25 wt% with the rest being the diluent toluene. Typically, to prepare an IPN with 30 wt% IIR rubber, a homogeneous solution was first obtained by dissolving 1.5 g of IIR in a mixture of C18A (3.5 g) and toluene (2 mL) at 80 °C for 8 h. After addition of Irgacure 2959 initiator (7 mg, 0.2 wt% with respect to C18A) under stirring, the homogeneous mixture was transferred between glass plates separated by a 1 mm spacer. After UV polymerization for 1 h at 30 ± 2 °C under UV light, IPNs formed were dried under vacuum to remove the diluent toluene.

### 4.2. Characterization

Thermal properties of IPNs were measured on a Perkin Elmer Diamond differential scanning calorimeter (DSC) under constant nitrogen flow. The samples loaded in hermetic pans were tested between 5 and 80 °C at a rate of 5 °C·min<sup>-1</sup> to determine the melting and crystallization temperatures, and the enthalpy of melting  $\Delta H_m$ . The crystallinity  $f_{cry}$  was determined by  $f_{cry} = w_{C18A} \Delta H_m / \Delta H_m^0$ , where  $w_{C18A}$  is the weight fraction of C18A units in the IPN,  $\Delta H_m^0$  is the melting enthalpy of 100% crystalline PC18A, taking the value of 219.4 J·g<sup>-1</sup> from the literature [53,54]. WAXS and SAXS experiments of IPNs were performed on a HECUS-SWAXS system (Graz, Austria) at 23 °C using Nickel filtered CuK<sub>α</sub> radiation ( $\lambda = 0.154$  nm) at 50 kV operating voltage and 40 mA current. The morphology of IPNs stained with Uranless was evaluated by transmission (TEM) and scanning transmission electron microscopy (STEM) on a JEOL ARM-200CF instrument operating at 200 kV, as detailed before [34]. The average size of the dispersed particles and the size distribution were determined by measuring the individual area of at least 90 particles from 20 independent TEM images at two different magnifications using the image processing software ImageJ (NIH, U.S. A.). From the areas of the particles, sphere-equivalent diameters of the particles, and the number- and weight- averages were calculated [34].

Rheological data were collected on a strain-controlled rheometer (Bohlin, Gemini 150, Malvern) connected with Peltier-temperature controller system. A parallel plate geometry was used with a diameter of 20 mm and a gap size of 1050 ± 85 μm depending on the thickness of the specimen. Cylindrical samples of 20 mm in diameter and ~ 1 mm in thickness were used for the measurements at a fixed strain amplitude  $\gamma_0$  of 0.1% in the linear regime. Frequency sweep was conducted from 0.3 to 300 rad·s<sup>-1</sup> while the heating-cooling cycles were performed at a frequency of 6.3 rad·s<sup>-1</sup>. The formation of IPNs was monitored using time-sweep measurements on a Physica MCR 302 Rheometer system (Anton Paar, Austria) equipped with an OmniCure 2000 curing system (UV light source).

Uniaxial tensile tests were performed at 23 ± 2 °C on a Zwick Roell test machine equipped with a 500 N load cell at a constant crosshead speed of 5 min<sup>-1</sup>. The flat specimens (20 × 30 × 1 mm<sup>3</sup>) and a gauge

length of 10 mm were used. Young's modulus  $E$  was determined from the linear region of the stress strain curves, i.e., between 0.01 and 2% deformations. The dissipated energy of IPNs was estimated by cyclic mechanical tests conducted at the same crosshead speed. The IPN specimens were loaded to a maximum strain  $\varepsilon_{max}$  of 500% strain and then unloaded for five successive cycles without a wait time between each cycle. The hysteresis energy  $U_{hys}$ , and the fraction of dissipated energy  $f_{diss}$  were calculated from loading ( $U_{load}$ ) and unloading ( $U_{unload}$ ) energies by,

$$U_{hys} = U_{load} - U_{unload} = \int_0^{\varepsilon_{max}} \sigma_{nom} d\varepsilon - \int_{\varepsilon_{max}}^0 \sigma_{nom} d\varepsilon \quad (2)$$

$$f_{diss} = U_{hys}/U_{load} \quad (3)$$

For the self-healing tests, IPN samples ( $20 \times 10 \times 1 \text{ mm}^3$ ) were first cut at their centers into two pieces with a sharp blade and then healed by putting the cut pieces together at  $65^\circ\text{C}$  for 24 h. After cooling, the mechanical behavior of healed specimens was tested as described above. Shape-memory tests on IPN samples of the same dimensions were conducted by a bending test. The samples were first deformed to a U-shape at  $65^\circ\text{C}$  and then quenched at  $25^\circ\text{C}$  to fix the temporary deformation angle  $\theta_d$ . The samples were then reheated to  $80\text{--}85^\circ\text{C}$  (an arbitrary temperature above  $T_m$ ) at steps of  $1\text{--}3^\circ\text{C}$  during which  $\theta_d$  is recorded by the image analyzing system Image-Pro Plus. The shape-recovery ratio  $R\theta$  was calculated as  $R\theta = \theta_d/180$ .

For the determination of the swelling ratio and sol fraction, IPN samples of dimensions  $40 \times 50 \times 1 \text{ mm}^3$  were weighed to determine the initial mass ( $m$ ), and then immersed in an excess of toluene for one week by refreshing toluene several times. They were weighed again to determine the swollen mass ( $m_s$ ), and then transferred to methanol which is a poor solvent for IPNs and facilitates their drying. After drying in a vacuum oven, the samples were weighed to determine the final mass  $m_{dry}$  of IPNs. The equilibrium degree of swelling  $q_w$  and the soluble fraction  $w_{sol}$  were calculated as  $q_w = m_s/m_{dry}$  and  $w_{sol} = 1 - m_{dry}/m$ , respectively.

#### Data availability

The raw/processed data required to reproduce these findings cannot be shared at this time as the data also forms part of an ongoing study.

#### CRedit authorship contribution statement

**Esra Su:** Methodology, Investigation, Formal analysis, Writing – original draft. **Gozde Bayazit:** Methodology, Investigation. **Semra Ide:** Methodology, Investigation. **Oguz Okay:** Methodology, Supervision, Writing – review & editing.

#### Declaration of Competing Interest

The authors declare that they have no known competing financial interests or personal relationships that could have appeared to influence the work reported in this paper.

#### Acknowledgements

This work was supported by the Scientific and Technical Research Council of Turkey (TUBITAK), MAG-218M502. O.O. thanks the Turkish Academy of Sciences (TUBA) for the partial support.

#### Appendix A. Supplementary material

Supplementary data to this article can be found online at <https://doi.org/10.1016/j.eurpolymj.2022.111098>.

#### References

- [1] J.E. Mark, B. Erman, Rubberlike Elasticity, Cambridge University Press, Cambridge, UK, 2007.
- [2] M. Hernández Santana, M. den Brabander, S. García, S. van der Zwaag, Routes to make natural rubber heal: A review, *Polym. Rev.* 58 (4) (2018) 585–609.
- [3] M. Behl, A. Lendlein, Shape-memory polymers and shape-changing polymers. Shape-memory polymers, *Adv. Polym. Sci.* 226 (2010) 1–40.
- [4] H.P. Xiang, H.J. Qian, Z.Y. Lu, M.Z. Rong, M.Q. Zhang, Crack healing and reclaiming of vulcanized rubber by triggering the rearrangement of inherent sulfur crosslinked networks, *Green Chem.* 17 (8) (2015) 4315–4325.
- [5] H.P. Xiang, M.Z. Rong, M.Q. Zhang, Self-healing, reshaping, and recycling of vulcanized chloroprene rubber: A case study of multitask cyclic utilization of cross-linked polymer, *ACS Sustainable Chem. Eng.* 4 (2016) 2715–2724.
- [6] M. Hernández, A.M. Grande, W. Dierkes, J. Bijleveld, S. van der Zwaag, S.J. García, Turning vulcanized natural rubber into a self-healing polymer: Effect of the disulfide/polysulfide ratio, *ACS Sustainable Chem. Eng.* 4 (10) (2016) 5776–5784.
- [7] M. Hernández, A.M. Grande, S. van der Zwaag, S.J. García, Monitoring network and interfacial healing processes by broadband dielectric spectroscopy: A case study on natural rubber, *ACS Appl. Mater. Interfaces* 8 (2016) 10647–10656.
- [8] M.A. Rahman, L. Sartore, F. Bignotti, L. Di Landro, Autonomic self-healing in epoxidized natural rubber, *ACS Appl. Mater. Interfaces* 5 (4) (2013) 1494–1502.
- [9] J. Huang, L. Cao, D. Yuan, Y. Chen, Design of novel self-healing thermoplastic vulcanizates utilizing thermal/magnetic/light-triggered shape memory effects, *ACS Appl. Mater. Interfaces* 10 (2018) 40996–41002.
- [10] X. Kuang, G.M. Liu, X. Dong, D.J. Wang, Enhancement of mechanical and self-healing performance in multiwall carbon nanotube/rubber composites via Diels-Alder bonding, *Macromol. Mater. Eng.* 301 (2016) 535–541.
- [11] M.M.A. Rabo Moustafa, E.R. Gillies, Rubber functionalization by Diels-Alder chemistry: From cross-linking to multifunctional graft copolymer synthesis, *Macromolecules* 46 (2013) 6024–6030.
- [12] P. Tanasi, M.H. Santana, J. Carretero-González, R. Verdejo, M.A. López-Manchado, Thermo-reversible crosslinked natural rubber: A Diels-Alder route for reuse and self-healing properties in elastomers, *Polymer* 175 (2019) 15–24.
- [13] Z. Feng, J. Hu, H. Zuo, N. Ning, L. Zhang, B. Yu, M. Tian, Photothermal-induced self-healable and reconfigurable shape memory bio-based elastomer with recyclable ability, *ACS Appl. Mater. Interfaces* 11 (2019) 1469–1479.
- [14] C. Xu, R. Cui, L. Fu, B. Lin, Recyclable and heat-healable epoxidized natural rubber/bentonite composites, *Compos. Sci. Technol.* 167 (2018) 421–430.
- [15] B. Cheng, X. Lu, J. Zhou, R. Qin, Y. Yang, Dual cross-linked self-healing and recyclable epoxidized natural rubber based on multiple reversible effects, *ACS Sustainable Chem. Eng.* 7 (2019) 4443–4455.
- [16] L. Cao, D. Yuan, C. Xu, Y. Chen, Biobased, self-healable, high strength rubber with tunicate cellulose nanocrystals, *Nanoscale* 9 (40) (2017) 15696–15706.
- [17] A.C. Schüssele, F. Nübling, Y.i. Thomann, O. Carstensen, G. Bauer, T. Speck, R. Mühlhaupt, Self-healing rubbers based on NBR blends with hyperbranched polyethylenimines, *Macromol. Mater. Eng.* 297 (5) (2012) 411–419.
- [18] A. Das, A. Sallat, F. Böhme, M. Suckow, D. Basu, S. Wiebner, K.W. Stockelhuber, B. Voit, G. Heinrich, Ionic modification turns commercial rubber into a self-healing material, *ACS Appl. Mater. Interfaces* 7 (2015) 20623–20630.
- [19] M. Suckow, A. Mordvinkin, M. Roy, N.K. Singha, G. Heinrich, B. Voit, K. Saalwächter, F. Böhme, Tuning the properties and self-healing behavior of ionically modified poly(isobutylene-co-isoprene) rubber, *Macromolecules* 51 (2018) 468–479.
- [20] M. Mordvinkin, M. Suckow, F. Böhme, R.H. Colby, C. Creton, K. Saalwächter, Hierarchical sticker and sticky chain dynamics in self-healing butyl rubber ionomers, *Macromolecules* 52 (2019) 4169–4184.
- [21] C. Xu, L. Cao, B. Lin, X. Liang, Y. Chen, Design of self-healing supramolecular rubbers by introducing ionic cross-links into natural rubber via a controlled vulcanization, *ACS Appl. Mater. Interfaces* 8 (27) (2016) 17728–17737.
- [22] C. Xu, L. Cao, X. Huang, Y. Chen, B. Lin, L. Fu, Self-healing natural rubber with tailorable mechanical properties based on ionic supramolecular hybrid network, *ACS Appl. Mater. Interfaces* 9 (34) (2017) 29363–29373.
- [23] C. Xu, X. Huang, C. Li, Y. Chen, B. Lin, X. Liang, Design of “Zn<sup>2+</sup> salt-bondings” cross-linked carboxylated styrene butadiene rubber with reprocessing and recycling ability via rearrangements of ionic cross-linkings, *ACS Sustainable Chem. Eng.* 4 (12) (2016) 6981–6990.
- [24] S.-M. Lai, J.-L. Liu, Y.-H. Huang, Preparation of self-healing natural rubber/polycaprolactone (NR/PCL) blends, *J. Macromol. Sci. Part B: Phys.* 59 (2020) 587–607.
- [25] Y. Cao, Y.J. Tan, S. Li, W.W. Lee, H. Guo, Y. Cai, C. Wang, B.-C.-K. Tee, Self-healing electronic skins for aquatic environments, *Nat. Electron.* 2 (2019) 75–82.
- [26] Y.-W. Chang, Shape-memory polymer blends, in: V. Mittal (Ed.), *Functional Polymer Blends. Synthesis, Properties, and Performance*, CRC, Taylor & Francis Group, Boca Raton, 2012, pp. 127–146.
- [27] K. Yu, A. Xin, Z. Feng, K.H. Lee, Q. Wang, Mechanics of self-healing thermoplastic elastomers, *J. Mech. Phys. Solids* 137 (2020) 103831.
- [28] V. Montano, M.M.B. Wempe, S.M.H. Does, J.C. Bijleveld, S. van der Zwaag, S. J. García, Controlling healing and toughness in polyurethanes by branch-mediated tube dilation, *Macromolecules* 52 (2019) 8067–8078.
- [29] C. Xu, J. Nie, W. Wu, Z. Zheng, Y. Chen, Self-healable, recyclable, and strengthened epoxidized natural rubber/carboxymethyl chitosan biobased composites with hydrogen bonding supramolecular hybrid networks, *ACS Sustainable Chem. Eng.* 7 (2019) 15778–15789.
- [30] H.H. Le, S. Hait, A. Das, S. Wiessner, K.W. Stockelhuber, F. Boehme, U. Reuter, K. Naskar, G. Heinrich, H.J. Radsch, Self-healing properties of carbon nanotube

- filled natural rubber/bromobutyl rubber blends. *EXPRESS Polym. Lett.* 11 (2017) 230–242.
- [31] J.-C. Kim, Y.-W. Chang, M. Sabzi, Designing self-crosslinkable ternary blends using epoxidized natural rubber (ENR)/poly(ethylene-co-acrylic acid) (EAA)/poly( $\epsilon$ -caprolactone) (PCL) demonstrating triple-shape memory behavior, *Eur. Polym. J.* 152 (2021) 110488.
- [32] M. Kashif, Y.-W. Chang, Triple-shape memory effects of modified semicrystalline ethylene-propylene-diene rubber/poly( $\epsilon$ -caprolactone) blends, *Eur. Polym. J.* 70 (2015) 306–316.
- [33] N.R. Brostowitz, R.A. Weiss, K.A. Cavicchi, Facile fabrication of a shape memory polymer by swelling cross-linked natural rubber with stearic acid, *ACS Macro Lett.* 3 (2014) 374–377.
- [34] E. Su, C. Bilici, G. Bayazit, S. Ide, O. Okay, Solvent-free UV polymerization of *n*-octadecyl acrylate in butyl rubber: A simple way to produce tough and smart polymeric materials at ambient temperature, *ACS Appl. Mater. Interfaces* 13 (2021) 21786–21799.
- [35] J.L. Lee, E.M. Pearce, T.K. Kwei, Morphological development in alkyl-substituted semiflexible polymers, *Macromolecules* 30 (1997) 8233–8244.
- [36] K. Ebata, Y. Hashimoto, S. Yamamoto, M. Mitsuishi, S. Nagano, J. Matsui, Nanophase separation of poly(*N*-alkyl acrylamides): The dependence of the formation of lamellar structures on their alkyl side chains, *Macromolecules* 52 (2019) 9773–9780.
- [37] C. Bilici, O. Okay, Shape memory hydrogels via micellar copolymerization of acrylic acid and *n*-octadecyl acrylate in aqueous media, *Macromolecules* 46 (2013) 3125–3131.
- [38] Y. Osada, A. Matsuda, Shape memory in hydrogels, *Nature* 376 (1995) 219.
- [39] A. Matsuda, J. Sato, H. Yasunaga, Y. Osada, Order-disorder transition of a hydrogel containing an *n*-alkyl acrylate, *Macromolecules* 27 (1994) 7695–7698.
- [40] C. Bilici, V. Can, U. Nöchel, M. Behl, A. Lendlein, O. Okay, Melt-processable shape-memory hydrogels with self-healing ability of high mechanical strength, *Macromolecules* 49 (2016) 7442–7449.
- [41] S. Majumder, R. Reiter, J. Xu, G. Reiter, Controlling the growth of stacks of correlated lamellar crystals of a block copolymer, *Macromolecules* 52 (2019) 9665–9671.
- [42] H. Guo, Y. Zhang, F. Xue, Z. Cai, Y. Shang, J. Li, Y. Chen, Z. Wu, S. Jiang, In-situ synchrotron SAXS and WAXS investigations on deformation and  $\alpha$ - $\beta$  transformation of uniaxial stretched poly(vinylidene fluoride), *CrystEngComm* 15 (2013) 1597–1606.
- [43] S. Humbert, O. Lame, J.-M. Chenal, C. Rochas, G. Vigier, Small strain behavior of polyethylene: In situ SAXS measurements, *J. Polym. Sci., Part B: Polym. Phys.* 48 (2010) 1535–1542.
- [44] K.-H. Nitta, M. Takayanagi, Novel proposal of lamellar clustering process for elucidation of tensile yield behavior of linear polyethylenes, *J. Macromol. Sci., Part B: Phys.* 42 (2003) 107–126.
- [45] K.-H. Nitta, M. Takayanagi, Role of tie molecules in the yielding deformation of isotactic polypropylene, *J. Polym. Sci., Part B: Polym. Phys.* 37 (4) (1999) 357–368.
- [46] K.-H. Nitta, M. Takayanagi, Tensile yield of isotactic polypropylene in terms of a lamellar-cluster model, *J. Polym. Sci., Part B: Polym. Phys.* 38 (8) (2000) 1037–1044.
- [47] J.P. Gong, Why are double network hydrogels so tough? *Soft Matter* 6 (2010) 2583–2590.
- [48] M.S. Silverstein, Interpenetrating polymer networks: So happy together? *Polymer* 207 (2020) 122929.
- [49] T. Ghosh, N. Karak, Tough interpenetrating polymer network of silicone containing polyurethane and polystyrene with self-healing, shape memory and self-cleaning attributes, *RSC Adv.* 8 (2018) 17044–17055.
- [50] A.M. Peterson, H. Kotthapalli, M.A.M. Rahmathullah, G.R. Palmese, Investigation of interpenetrating polymer networks for self-healing applications, *Compos. Sci. Technol.* 72 (2012) 330–336.
- [51] C.S. Patrickios, K. Matyjaszewski, Amphiphilic polymer co-networks: 32 years old and growing stronger—a perspective, *Polym. Int.* 70 (2021) 10–13.
- [52] G. Kali, T.K. Georgiou, B. Ivan, C.S. Patrickios, E. Loizou, Y. Thomann, J.C. Tiller, Synthesis and characterization of anionic amphiphilic model conetworks based on methacrylic acid and methyl methacrylate: Effects of composition and architecture, *Macromolecules* 40 (2007) 2192–2200.
- [53] Z. Mogri, D.R. Paul, Gas sorption and transport in side-chain crystalline and molten poly(octadecyl acrylate), *Polymer* 42 (2001) 2531–2542.
- [54] H.S. Bisht, P.P. Pande, A.K. Chatterjee, Docosyl acrylate modified polyacrylic acid: Synthesis and crystallinity, *Eur. Polym. J.* 38 (12) (2002) 2355–2358.